Microelectronic Engineering 192 (2018) 88–95

Contents lists available at ScienceDirect

Microelectronic Engineering

journal homepage: www.elsevier.com/locate/mee

Research paper

Laser micromachining of tapered optical fibers for spatially selective control of neural activity

Alessandro Rizzo [a,b,*], Enrico Domenico Lemma [a,b], Filippo Pisano [a], Marco Pisanello [a], Leonardo Sileo [a], Massimo De Vittorio [a,b,1], Ferruccio Pisanello [a,*,1]

[a] Istituto Italiano di Tecnologia (IIT), Center for Biomolecular Nanotechnologies, Via Barsanti snc, 73010 Arnesano, Italy
[b] Dipartimento di Ingegneria dell'Innovazione, Università del Salento, via per Monteroni, 73010 Lecce, Italy

ARTICLE INFO

Article history:
Received 21 October 2017
Received in revised form 6 February 2018
Accepted 8 February 2018
Available online 09 February 2018

Keywords:
Direct laser writing
Tapered fiber
Coupling angle
Ablation
Laser micromachining

ABSTRACT

Tapered and micro-structured optical fibers (TFs) recently emerged as a versatile tool to obtain dynamically addressable light delivery for optogenetic control of neural activity in the mammalian brain. Small apertures along a metal-coated and low-angle taper allow for controlling light delivery sites in the neural tissue by acting on the coupling angle of the light launched into the fiber. However, their realization is typically based on focused ion beam (FIB) milling, a high-resolution but time-consuming technique. In this work we describe a laser micromachining approach to pattern TFs edge in a faster, more versatile and cost-effective fashion. A four-axis piezoelectric stage is implemented to move and rotate the fiber during processing to realize micropatterns all-around the taper, enabling for complex light emission geometries with TFs.
© 2018 The Authors. Published by Elsevier B.V. This is an open access article under the CC BY-NC-ND license (http://creativecommons.org/licenses/by-nc-nd/4.0/).

1. Introduction

The advent of optogenetics to trigger neural activity in vivo [1] has generated a new class of hardware technologies to better interface with the brain [2–6]. Most of these methods aim at overcoming the limitations given by light delivery based on flat-cleaved optical fibers, i.e. producing severe implant damage and illumination of a small and fixed brain volume. Promising approaches to reduce invasiveness and to dynamically switch illumination between several regions of the brain are represented by multiple micro light emitting diodes (μLEDs) [7–9], holographic illumination via head-mounted objectives [10] GRIN lenses [11] and tapered optical fibers (TFs) [12–14].

TFs are advantageous because they can generate both wide-volume light delivery and site-selective optical control of neural activity [15,16]. Also, the photonic properties of the fiber taper can be exploited to engineer minimally invasive multipoint emitting tapered fibers (MPFs) that can switch illumination between different, localized regions of the brain [13–15]. This has been obtained by coating the tapered region with a reflective metal layer and then opening micrometer-sized apertures with Focused Ion Beam (FIB) milling to define several light-emitting windows [13]. Being placed at specific sections of the taper, each of these windows can be independently activated by exploiting mode division de-multiplexing [14]. This, in turn, results in a single device that provides for reconfigurable light-delivery in multiple brain regions [14].

However, the fabrication process to obtain MPFs presents a critical step: the realization of optical windows on the non-planar, small curvature radius surface of the taper. Focused Ion Beam (FIB) milling has been previously employed as it allows fabrication with a resolution of a tens of nanometers [13], much lower than the taper's radius of curvature where the patterning is usually performed (~5 μm) [13,14,17]. However, FIB milling becomes not practical for the realization of structures exceeding a few hundreds of micrometers, due to (i) the long processing time and (ii) the need to stitch geometries exceeding the available field of view. While this latter induces unavoidable imperfections in the milled geometry, the time required to mill large patterns limits the overall throughput. Indeed, the realization of a $20 \times 20 \mu m^2$ optical window can require up to 0.5 h of continuous milling, while a 3.5 h processing time is required for realizing a taper with 7 windows arranged over a 1 mm length [13]. These drawbacks, in combination with the high cost of the equipment to implement FIB milling, represented an obstacle to the potential diffusion of the MPF technology.

This work proposes laser micromachining as an alternative to FIB milling for faster, more versatile and cost-effective realization of micro-patterns on the highly-curved surface of TFs' edge. With respect to other Direct Laser Writing (DLW) systems used to realize patterns on non-tapered optical fibers [18], a 4-axis (x-y-z-Φ) piezoelectric stage is implemented to have the fiber rotating around its axis during

* Corresponding authors.
E-mail addresses: alessandro.rizzo@iit.it (A. Rizzo), ferruccio.pisanello@iit.it (F. Pisanello).
[1] M.D.V. and F. Pisanello equally contributed to this work.

https://doi.org/10.1016/j.mee.2018.02.010
0167-9317/© 2018 The Authors. Published by Elsevier B.V. This is an open access article under the CC BY-NC-ND license (http://creativecommons.org/licenses/by-nc-nd/4.0/).

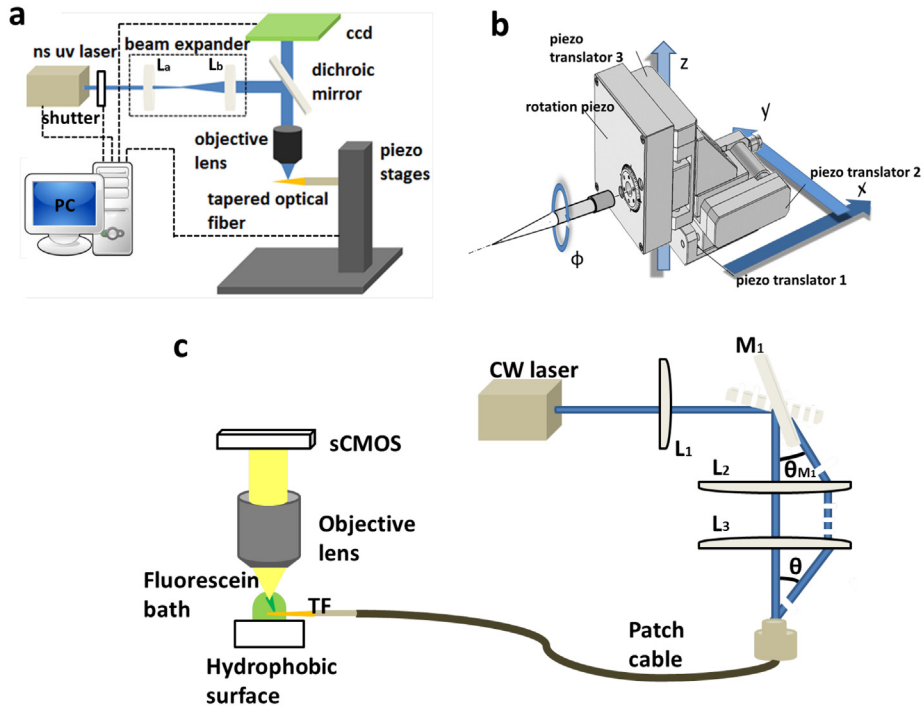

Fig. 1. (a) Diagram of the DLW system. A UV ns pulsed laser is expanded by lenses L_a (focal length f1 = 60 mm) and L_b (f2 = 250 mm), reflected by a dichroic mirror and focused by a microscope objective on the taper edge. A CCD camera captured a live view of the TF mounted on a computer-controlled x-y-z-φ piezoelectric (see axis definition in Fig. 1b) (b) Schematic of the piezoelectric stage. Three single-axis translation stages were combined with a rotational stage to control the movement of the TF that was mounted coaxially to the rotation stage. (c) Optical setup used to change light injection angle θ while observing emission from the taper in a PBS: Fluorescein solution with a sCMOS camera.

exposure to a UV ablation beam. This approach enables the realization of complex geometries all around the taper, extending the possible light emission patterns that can be generated with TFs.

2. Materials and methods

TFs were provided by OptogeniX (www.optogenix.com) and were realized starting from 0.39 NA optical fibers with 200/225 core/cladding diameters. To coat the TFs with a ~600 nm-thick aluminum (Al) or gold (Au) layer, the chamber of a thermal evaporation system was modified by introducing a stepper motor and a custom holder to have several fibers rotating during the evaporation process (see scheme in Fig. S1) [17].

Patterns on the metal coating were obtained with the setup displayed in Fig. 1a, using a 10 ns-pulsed laser (Spectra Physics Explorer, $\lambda = 349$ nm, tunable repetition rate in the range 1 Hz–4 MHz) at $\lambda = 349$ nm, which was expanded with two converging lenses (L_a and L_b with focal length $f_a = 60$ mm and $f_b = 250$ mm, Thorlabs LA1401-A and LA1301-A, respectively). The laser beam was focused on the sample by a 0.90NA microscope objective (Olympus, Uapo340, 40×) with a theoretical waist of ~485 nm. The TF was connected to a four-axis piezo mover (PI GmbH, Q-545.140 and U-628.03) by a custom fiber holder, allowing for translation along x, y and z and rotation around the taper axis (see Fig. 1b). The overall system was controlled by LabView.

Light emission from the patterned TFs was tested with the optical setup depicted in Fig. 1c: a 2 mW $\lambda_0 = 473$ nm beam (Laser Quantum Ciel 473) passes through lens L_1 (focal length $f_1 = 100$ mm, Thorlabs LA1050-A) and is focalized on the surface of a galvanometric mirror M_1 (Sutter RESSCAN-MOM); light reflected from M_1 is then collimated by lens L_2 ($f_2 = 100$ mm, Thorlabs AL50100-A). The laser beam is focused by lens L_3 ($f_3 = 32$ mm, Thorlabs AL4532-A) into the fiber with an input coupling angle $\theta = \tan^{-1}(f_2 \cdot f_3^{-1} \cdot \tan\theta_{M1})$ depending on the deflection θ_{M1} induced on the beam by the galvanometric mirror inclination. TFs were connected to the setup by a ferrule-to-ferrule butt coupling and immersed in a PBS:fluorescein bath. The fluorescence images were collected by an optical microscope (Scientifica Slicescope) equipped with a 4× objective lens (Olympus XLFluor 4×/340) and a sCMOS sensor (Hamamatsu ORCA-Flash4.0 v2). Emission profiles were evaluated over a line placed next to the taper. The extinction ratio was defined as the ratio between light intensity emitted from the active window divided by the light intensity emitted from a non-active window.

3. Results

3.1. Direct laser writing on a tapered optical fiber

The DLW experimental setup developed in this work is summarized in Fig.1a. The pulsed $\lambda = 349$ nm laser was directed to the back aperture of the 0.90 NA objective, which focuses the radiation on the TF and locally ablates the metal coating. A software-driven shutter was used to control exposure time. The x-y-z-Φ piezoelectric stage moves the tapered fiber with respect to the objective's focal spot (Fig. 1b). Control on Φ allows to realize patterns all around the tapered fiber and to precisely move the taper surface following the designed patterns. Eccentric fiber rotations can be compensated by fine adjustment of the y-z position, therefore assuring an accurate alignment between the point to be ablated and the objective focal spot, apart from the small angle in the x-z plane introduced by the waveguide narrowing. Both Au and Al metal coatings were tested. Al was chosen by virtue of its high reflectivity at both $\lambda = 473$ nm and $\lambda = 593$ nm, two wavelengths commonly used to excite or inhibit action potential generation [19], although it is not suitable for chronic implants since it induces neurotoxicity by accelerating oxidative damage to biomolecules [20]. Au can instead be used by virtue of its higher biocompatibility, although it has a lower reflectivity at 473 nm and a higher cost of the raw material.

To estimate the minimum feature size that the system can ablate on the fiber edge, single-point exposure was performed as a function of

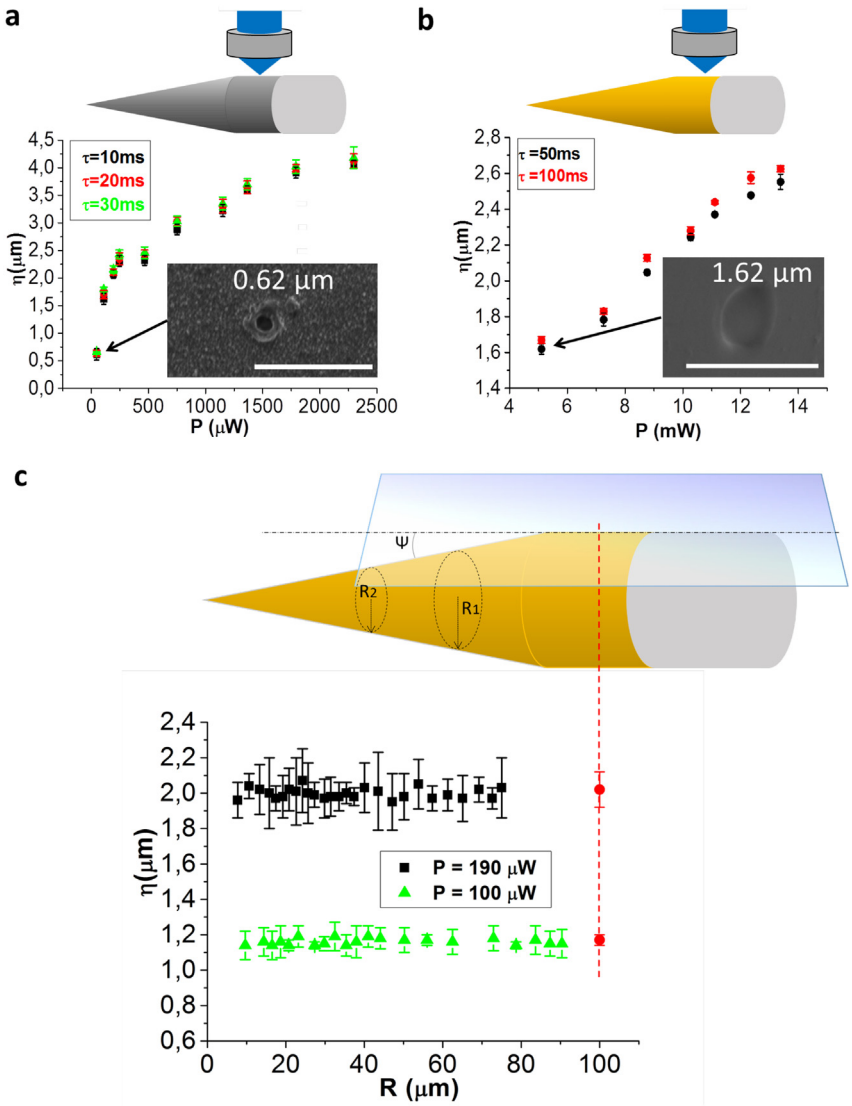

Fig. 2. (a, b) Diameter of the realized spot η as a function of laser power P for different exposure times and for both Al (panel a) and Au (panel b) coatings. The insets show the obtained ablation spots at the minium power used to evaluate η_{MIN}. Insets scale bars represent 5 μm. Data are represented as mean ± standard deviation on $N = 10$ exposures (c) (Top) Schematic representation of the fiber taper and relevant definitions, i.e. Ψ taper angle and radius of curvature. Radius of curvature R_i is defined as the radius of the circular section obtained sectioning the fiber with a plane normal to the fiber axis. (Bottom)The graph shows η as a function of R for laser powers of $P = 190$ μW (black points) and $P = 100$ μW (green points), both at exposure times of $\tau = 10$ ms. The red dots represent spots written on the non-tapered section of the fibers ($R = 100$ μm). (For interpretation of the references to colour in this figure legend, the reader is referred to the web version of this article.)

laser power (P) and exposure time (τ). This results in almost circular ablation spots as shown in Fig. 2a and b for both Al and Au coatings, although the obtained patter for Au is slightly more elliptic. To avoid the influence of the taper angle (Ψ, defined in Fig. 2c), this evaluation was carried out on the non-tapered region of waveguide. For both metals, the diameter of the realized spots (η) increases as a function of P. In the case of the Al-coated fiber η increases as a function of the laser power: the smallest feature $\eta_{MIN} = 0.6 \pm 0.2$ μm was obtained for $P = 47 \pm 1$ μW and $\tau = 10$ ms. Au-coating resulted to be harder to remove; therefore, higher powers (from $P \approx 5.1$ mW to $P \approx 13.4$ mW) and longer exposure times ($\tau = 50$ ms and $\tau = 100$ ms) were tested. In this case, the $\eta_{MIN} = 1.6 \pm 0.1$ μm was obtained for $P = 5.10 \pm 0.04$ mW and $\tau = 50$ ms. As the taper narrows, the system deviates from the ideal conditions used to evaluate η, for two main reasons: a tilt offset along x is introduced by the taper angle and the radius of curvature decreases moving closer to the tip (Fig. 2c). However, this has no significant effect on η: as shown Fig. 2c for two different exposure conditions ($P = 100$ μW and $P = 190$ μW, $\tau = 10$ ms), η is almost constant as a function of the distance from the taper tip, mostly because the spot size remains much lower than the radius of curvature R (tested in the range from $R = 7$ μm to $R = 75$ μm). Since the condition $\eta_{MIN} << R$ is verified for both metal coatings, in the following we only describe patterning of Al-coated fibers, but the obtained results can be straightforwardly extended also to the Au coating.

Three different patterning geometries are described in the following paragraphs: the realization of square optical windows for site-selective light delivery, annular patterning all-around the taper to obtain emission with a cylindrical symmetry, and the realization of slot apertures along the taper for light emission restricted on single side of the taper.

3.2. Realization of light delivery windows on the taper edge

With a laser power $P = 190$ μW, square optical apertures were realized along the fiber at three different taper diameters, chosen to have the relative distances between the apertures approximatively matching with the layered structure of mouse motor cortex (Fig. 3a). As shown in

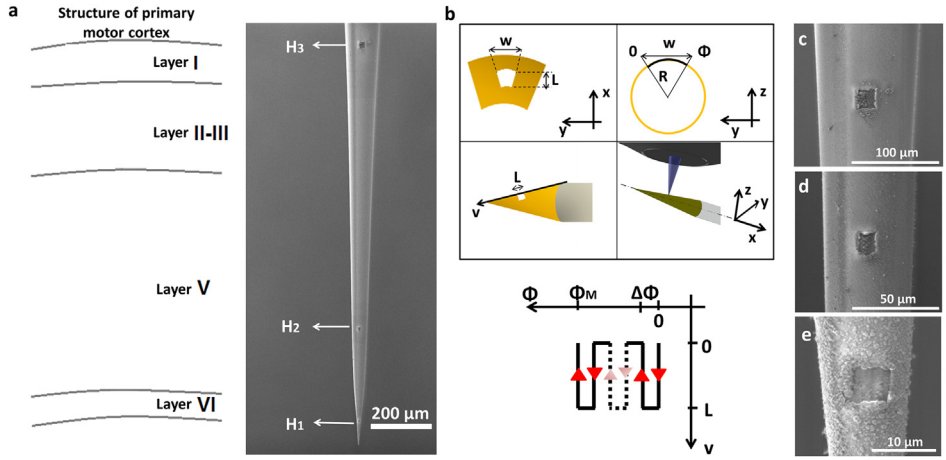

Fig. 3. (a) Schematic representation of primary motor cortex of the mouse brain (left) and SEM micrograph of the three-window device (right). The three windows are labeled as H1, H2, and H3. (b) Different views of the patterned geometry and definition of axes and sizes (Top). (Bottom) Schematic representation of the implemented raster scan to obtain a LxW window along the v and Φ. (c–e) SEM micrographs of H_3, H_2 and H_1, respectively.

the schematic representation in Fig. 3b, *L x W* windows were patterned by a bidirectional raster scan along *v* and *Φ* respectively, with *v* representing the axis defined by the taper edge and Φ representing the rotation angle of the fiber during patterning. The maximum rotation Φ_M needed to pattern a window of width W around the taper is function of the radius of curvature R, e.g. $\Phi_w = w/R$ (in radians). The raster scanning was performed with continuous exposure at a velocity of ~10 µm/s along *x* and *ΔΦ ~0.5°* steps along *Φ*, while compensating for eccentric rotations with pre-calibrated adjustments in the *y-z* plane. To completely remove the metal, exposure was performed twice on each window. Fig. 3c–e show SEM images of the three windows realized at diameters $a_1 \approx 15$ µm, $a_2 \approx 50$ µm and $a_3 \approx 110$ µm with sizes $L \times W$ of $5 \times 5\mu m^2$, $10 \times 10\mu m^2$ and $20 \times 20\mu m^2$, respectively. Fabrication times were 3 s for the smallest window, 6 s for the $10 \times 10\mu m^2$ window and 12 s for the $20 \times 20\mu m^2$ window, notably shorter than those obtained with FIB milling [13], which required at least a 30 min-long process for windows of the same size.

The main feature of the realized device is the possibility to selectively activate light delivery from each window by injecting light at the other end of the fiber with a specific input angle θ. This is possible

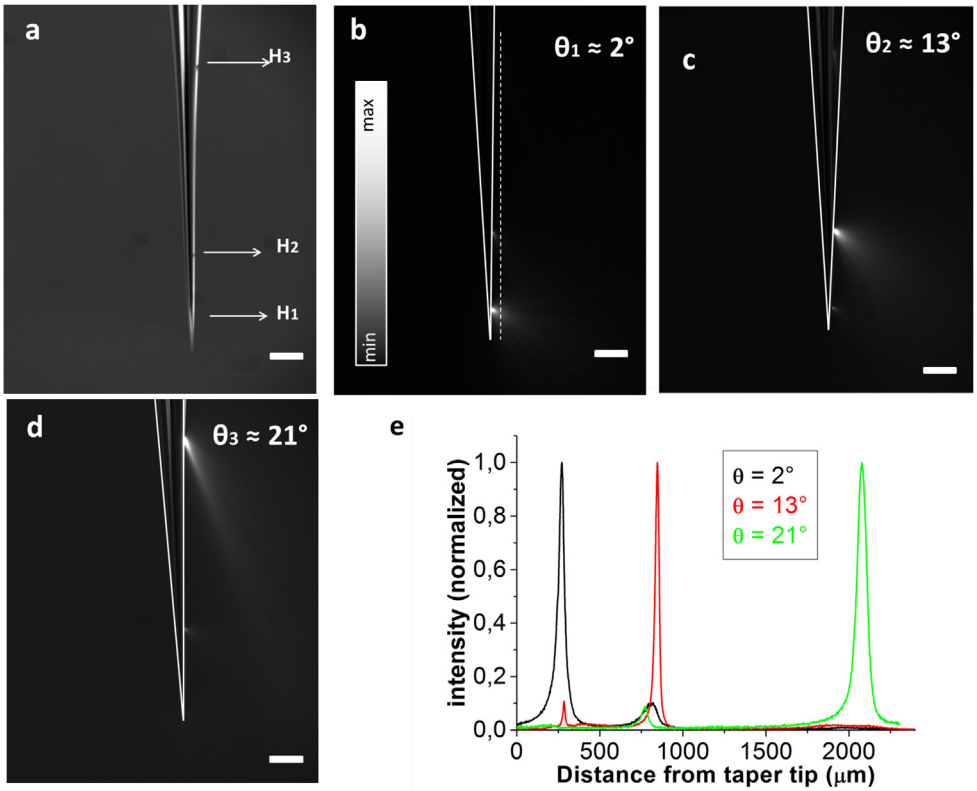

Fig. 4. (a) Bright-field image of the three-window device. Scale bar represents 200 µm. (b, c, d) Fluorescence images of the taper emission by setting three different input-coupling angles ($\theta_1 = 2°$, $\theta_2 = 13°$, $\theta_3 = 21°$ in panel b, c, and d, respectively). The white continuous lines represent the taper edges. The white dashed line represents the region over which the light intensity profiles in panel e were acquired. Scale bars represent 200 µm. (e) Intensity profiles collected along the white dashed line displayed in panel c. Black, red and green curves represent the emission profiles from $\theta = 2°$, $\theta = 13°$ and $\theta = 21°$, respectively. (For interpretation of the references to colour in this figure legend, the reader is referred to the web version of this article.)

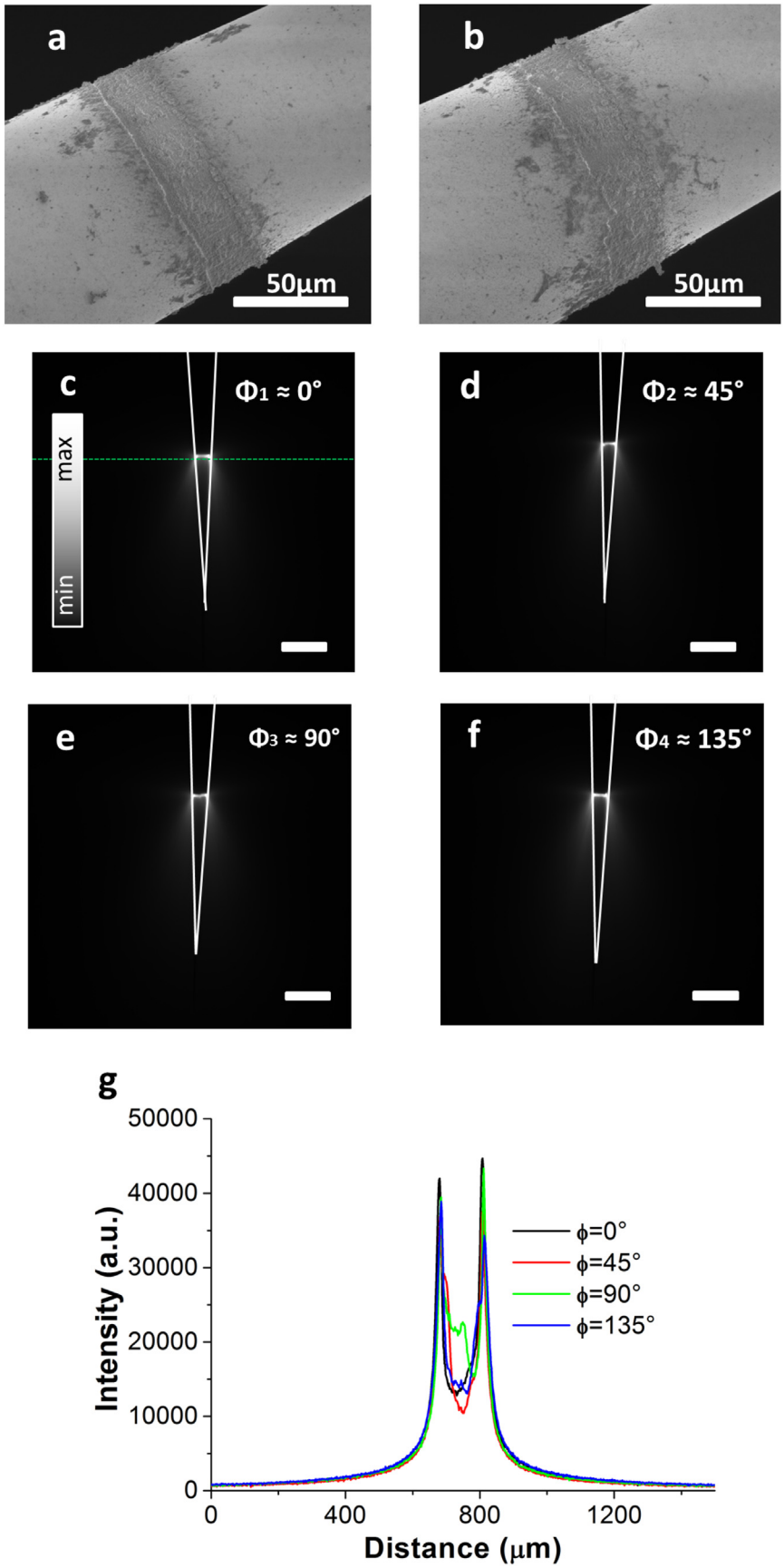

Fig. 5. (a, b) SEM images of the pattern ring-shaped window. The two images show two opposite sides of the taper (e.g. $\phi = 0$ and $\phi = 180°$). (c, d, e, f) Fluorescence images of the taper emission from four different sides of the taper ($\phi_1 = 0°$, $\phi_2 = 45°$, $\phi_3 = 90°$ and $\phi_4 = 135°$) Scale bars represent 200 μm. Taper edges are highlighted by the white continuous lines. (g) Overlay of the Intensity profiles collected along normal direction to the fiber optical axis (green dashed line in panel c). (For interpretation of the references to colour in this figure legend, the reader is referred to the web version of this article.)

because each of the three apertures can out-couple a specific modal subset into the environment, while by changing θ, only the specific modes emitted by the selected window are injected into the taper [13,14]. In order to characterize the optical properties of the device, we set up the optical path depicted in Fig. 1c and described in detail in the Materials and Methods section. The fiber taper was immersed in a PBS:Fluorescein solution and the resulting fluorescence was used to visualize optical emission from the taper edge, as displayed in Fig. 4a–d. At low input angles ($\theta_1 \approx 2°$) light is mostly emitted by the window closest to the tip (H_1), while increasing θ emission moves to window H_2 (at $\theta_2 \approx 13°$) and to window H_3 at ($\theta_3 \approx 21°$). By measuring the emission profiles from the three input angles, reported in Fig. 4e, we assessed emission selectivity from each window finding an extinction ratio >10:1 for all experiments (see Materials and Methods for extinction ratio definition).

3.3. Realization of annular windows

As discussed in the previous paragraph, square windows allow for site-selective light delivery at different taper sections. However, this geometrical configuration limits emission of light to a restricted angular width around the taper circumference, as identified by φ_W. Some brain structures, such as cortical layers, would instead benefit of a 360° symmetrical emission, which would be able to engage cells all around the waveguide. We therefore optimized a process to realize annular apertures (hereafter referred to as rings) at specific diameters around the taper by exploiting a rotational control of the fiber holder. As for square windows, a bi-directional raster scan was used with continuous exposure. With reference to axes and symbols defined in Fig. 3b, the fiber was moved along *v* for a length of L = 25 μm at a velocity of 10 μm/s and rotated of $\Delta\varphi = 0.5°$ with $\varphi_W = 1080°$, resulting in three 360° rotations to remove the metal coating. This allowed to remove metal coating on a surface area of 8635 μm^2 in only 700 s, while milling the same area with FIB milling would have required a 13,5 h-long process. A typical result of the fabrication process is displayed in Fig. 5a and b, showing two opposite sides of a ring aperture realized at a fiber diameter of 110 μm. Emission from the ring was tested in a PBS:fluorescein bath with the setup displayed in Fig. 1c by rotating the fiber around its axis and shown for $\Phi = 0°$, $\Phi = 45°$, $\Phi = 90°$ and $\Phi = 135°$ in Fig. 5c–f. To verify the emission homogeneity around the aperture, emission profiles on a line perpendicular to the optical axis across the ring (see dashed line in Fig. 5c) were measured from the same images and overlapped in the graph displayed in Fig. 5g. As the fiber is rotated, the overall shape and intensity of the profiles is preserved and the maximum recorded mismatch between intensity peaks was found to be below 20%.

To show that also this unconventional window shape allows for multisite light delivery, two rings (S_1 and S_2) with different lengths (L_1 ~ 15 μm and L_2 ~ 25 μm) were realized at taper sections with diameters a_1~13 μm and a_2~55 μm, respectively. As shown in Fig. 6a–b, each ring can be selectively activated by acting on θ: for $\theta \approx 2°$ only the ring closer to the taper tip emits light (extinction ratio 20:1), while for $\theta \approx 22°$ only the ring farther from the taper tip delivers light (extinction ratio 15:1).

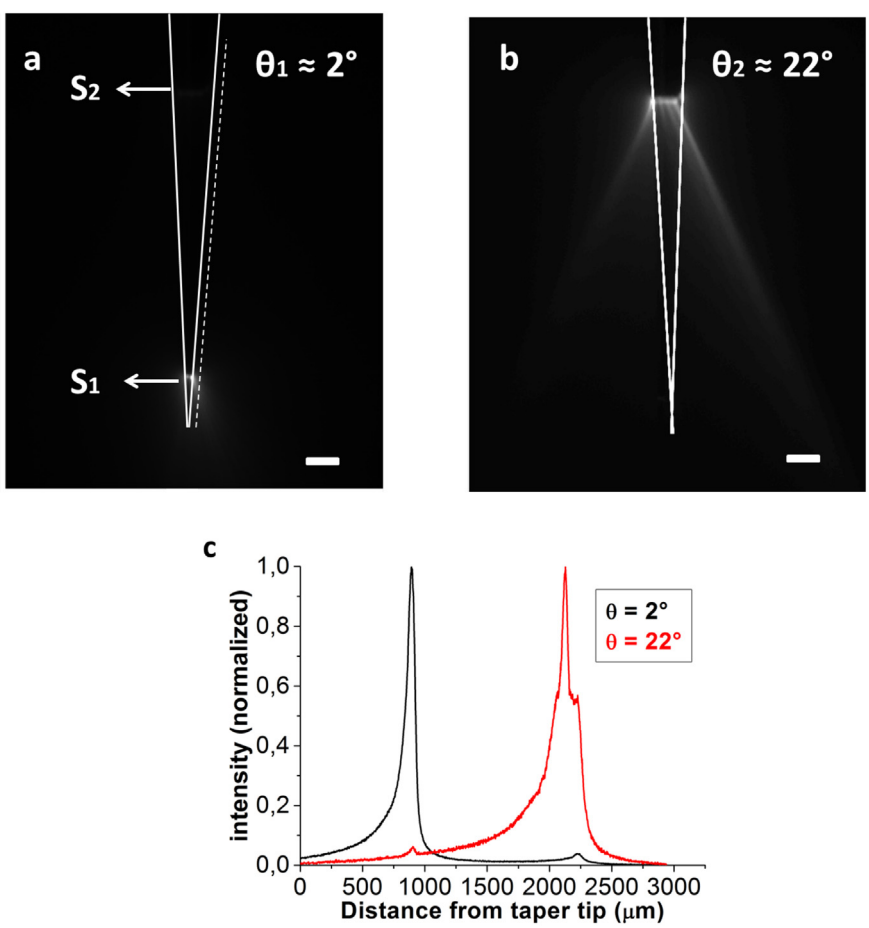

Fig. 6. (a, b) Emission from the two rings realized along the taper for two different input angles ($\theta_1 = 2°$, $\theta_2 = 22°$ in panel a and b, respectively). Scale bars represent 100 μm. The white continuous lines outline the taper edges. (c) Intensity profiles collected along the white dashed line displayed in panel a.

3.4. Single slot device

An important advantage of the DLW method proposed in this work with respect to FIB milling is the processing time and the possibility to realize wider patterns without field stitching. This enables the realization of large optical windows that can generate uniform light delivery in an extended wide volume of tissue, overtaking one of the main limitations of fiber optics used in optogenetics experiments.

An example of this is the fabrication of a 1 mm-long slot-line, shown in Fig. 7a–b, realized as a rectangular window with W x L ≈ 4 μm × 1000 μm. Processing time for the 1 mm slot was about t ≈ 200 s, while the same device would have required approximately 1 h with FIB milling. Through SEM inspection, we verified that the line width W remains constant along the whole patterned length to a value of 4.16 ± 0.14 μm. To characterize optical emission of the device, light was injected by filling the whole fiber NA, generating light emission from the entire slot (see Fig. 7c) with a relatively uniform emission profile (Fig. 7d). As shown in Fig. 7b, the SEM inspection also revealed a roughness of the silica underlying the Au coating, which, however, does not significantly alter the uniformity of the emitted light pattern. This roughness also depends on the laser power used during exposure and it is expected to slightly increase when patterning metals requiring higher exposure power and times.

4. Discussions and conclusions

This work describes a DLW approach to realize complex geometries on metal-coated tapered fibers for patterned light delivery into the brain, representing a cost-effective and faster alternative to FIB milling so far implemented to obtain the same devices. When compared with the FIB-based approaches [13,14], DLW has the clear advantage of shorter fabrication times, but also the clear disadvantage of a limited resolution. Realizing DLW patterns with sub-micrometer features would require a higher NA objective and a finer control of the exposure power density to avoid the generation of local heat, which could unavoidably alter the geometry of the ablated spots also at resolutions above the diffraction limit. FIB milling allows instead patterning with resolution in the order of ~50 nm all-along the taper [13]. Also, control on the depth of the written geometry is better done with FIB milling, by virtue of the higher resolution and the possibility to perform simultaneous SEM inspection during processing.

Although the use of laser ablation cannot compete with FIB in terms of resolution, the implementation of piezo-based translation and axial rotation of the taper allows the patterning of optical apertures around and along the taper, within the resolution limits given by the minimum feature size (η_{MIN}) that can be ablated by the focused laser spot. For the used system, η_{MIN} was found to be $\eta_{MIN} = 0.6 \pm 0.2$ μm and $\eta_{MIN} = 1.6 \pm 0.1$ μm for Al- and Au-coated fibers, respectively. These two coatings were chosen as representative cases because they represent two good candidates for acute (Al) and chronic (Au) implants. However, the here-proposed technique can be simply extended to any other reflective coating that can be deposited around the taper and that can be processed with DLW [21,22]. We observed that the ablated feature size obtained on an almost planar surface is preserved at taper diameters with radius of curvature as small as ≈5 μm, enabling the realization of a wide variety of patterns with processing times in the order of a few tens of seconds. This was shown by realizing different patterns that can target different regions of the brain. To obtain layer-selective light delivery in primary motor cortex (Fig. 3), three square apertures on the taper edge were realized at 80 μm, 390 μm and 1300 μm from the tip (patterning time t ≈ 10s for each window). Being patterned at a specific section of the taper, each window can be independently activated by injecting into the fiber a specific subset of guided modes, as shown in Fig. 4. To allow for emission with 360° symmetry, the fiber was rotated around its axis during processing, allowing to obtain the ring-shaped apertures shown in Fig. 5 (t ≈ 700 s). Also in this case, site

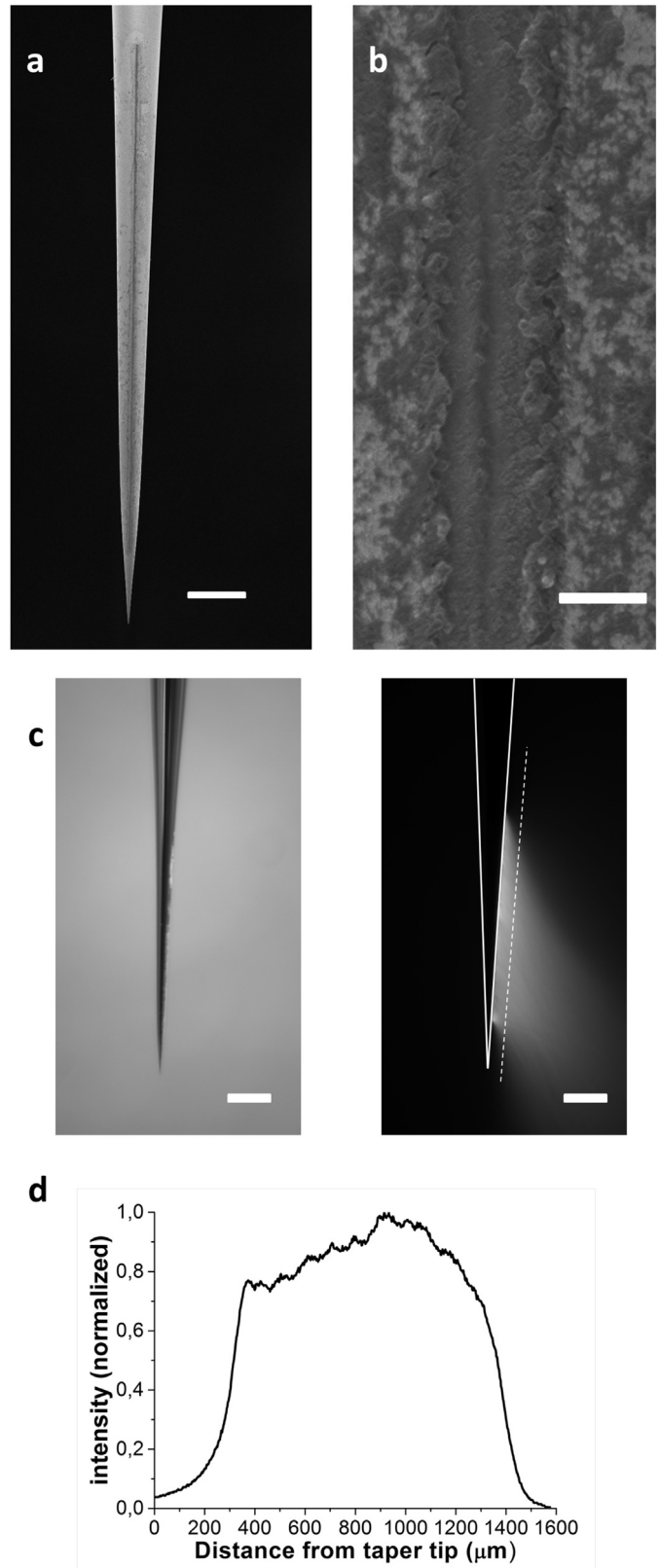

Fig. 7. (a, b) SEM micrographs of the single-slot device at two different magnifications. Scale bar represents 300 μm in panel a and 4 μm in panel b. (c) Bright-field (left) and emission (right) images of the single-slot device immersed in a drop of fluoresce. The white continuous lines outlines the taper edges. Scale bars represent 200 μm. (d) Intensity profile collected along the white dashed line displayed in panel c.

selective light delivery can be obtained if several rings are patterned at different sections of the taper (Fig. 6). With the goal of widening the illuminated volume of the brain, a third device was developed, consisting of a slot-like aperture along the taper and resulting in a relatively uniform illumination extending for ≈1 mm (patterning time was about t ≈ 200 s). The high versatility of the approach allows for the realization of virtually any micrometer-sized geometry around the taper in a speedy and cost-effective fashion with respect FIB milling. In this sense, the DLW approach can be preferred to FIB to realize patterned light delivery into the brain with tapered optical fibers.

Supplementary data to this article can be found online at https://doi.org/10.1016/j.mee.2018.02.010.

Acknowledgments

F. Pisanello and F. Pisano acknowledge funding from the European Research Council under the European Union's Horizon 2020 research and innovation program (#677683); M.P. and M.D.V. acknowledge funding from the European Research Council under the European Union's Horizon 2020 research and innovation program (#692943). L.S., M.D.V. are funded by the US National Institutes of Health (U01NS094190).

M. D. V. and F. Pisanello equally contributed to the work.

References

[1] E.S. Boyden, F. Zhang, E. Bamberg, G. Nagel, K. Deisseroth, Millisecond-timescale, genetically targeted optical control of neural activity, Nat. Neurosci. 20058 (9) (2005) 1263–1268.
[2] A.N. Zorzos, J. Scholvin, E.S. Boyden, C.G. Fonstad, Three-dimensional multiwaveguide probe array for light delivery to distributed brain circuits, Opt. Lett. 201237 (23) (2012) 4841–4843.
[3] K.Y. Kwon, H.-M. Lee, M. Ghovanloo, A. Weber, W. Li, Design, fabrication, and packaging of an integrated, wirelessly-powered optrode array for optogenetics application, Front. Syst. Neurosci. 20159 (2015) 69.
[4] M.R. Warden, J.A. Cardin, K. Deisseroth, Optical neural interfaces, Annu. Rev. Biomed. Eng. 201416 (1) (2014) 103–129.
[5] F. Pisanello, L. Sileo, M. De Vittorio, Micro- and nanotechnologies for optical neural interfaces, Front. Neurosci. 201610 (2016) 70.
[6] C. Yong Ku, Z. Guoan, J.A. George, H. Daniel, C. Adam, K. Thomas, P. Ferruccio, S.P. Francesco, M.V. Ivo, J.B. Martin, H. Song, Z. Jiang, C. Zhongping, H. Yoko, Roadmap on neurophotonics, J. Opt. 201618 (9) (2016), 093007.
[7] N. McAlinden, E. Gu, M.D. Dawson, S. Sakata, K. Mathieson, Optogenetic activation of neocortical neurons in vivo with a sapphire-based micro-scale LED probe, Frontiers in Neural Circuits 20159 (2015) 25.
[8] J.G. McCall, T.-i. Kim, G. Shin, X. Huang, Y.H. Jung, R. Al-Hasani, F.G. Omenetto, M.R. Bruchas, J.A. Rogers, Fabrication of flexible, multimodal light-emitting devices for wireless optogenetics, Nat. Protoc. 20138 (12) (2013) 2413–2428.
[9] R. Scharf, T. Tsunematsu, N. McAlinden, M.D. Dawson, S. Sakata, K. Mathieson, Depth-specific optogenetic control in vivo with a scalable, high-density μLED neural probe, Sci. Rep. 20166 (2016), 28381.
[10] V. Szabo, C. Ventalon, V. De Sars, J. Bradley, V. Emiliani, Spatially selective holographic photoactivation and functional fluorescence imaging in freely behaving mice with a fiberscope, Neuron 201484 (6) (2014) 1157–1169.
[11] C. Moretti, A. Antonini, S. Bovetti, C. Liberale, T. Fellin, Scanless functional imaging of hippocampal networks using patterned two-photon illumination through GRIN lenses, Biomed. Opt. Express 20167 (10) (2016) 3958–3967.
[12] E. Stark, T. Koos, G. Buzsáki, Diode probes for spatiotemporal optical control of multiple neurons in freely moving animals, J. Neurophysiol. 2012108 (1) (2012) 349.
[13] F. Pisanello, L. Sileo, Ian A. Oldenburg, M. Pisanello, L. Martiradonna, John A. Assad, Bernardo L. Sabatini, M. De Vittorio, Multipoint-emitting optical fibers for spatially addressable in vivo optogenetics, Neuron 201482 (6) (2014) 1245–1254.
[14] M. Pisanello, A. Della Patria, L. Sileo, B.L. Sabatini, M. De Vittorio, F. Pisanello, Modal demultiplexing properties of tapered and nanostructured optical fibers for in vivo optogenetic control of neural activity, Biomed. Opt. Express 20156 (10) (2015) 4014–4026.
[15] F. Pisanello, G. Mandelbaum, M. Pisanello, I.A. Oldenburg, L. Sileo, J.E. Markowitz, R.E. Peterson, A. Della Patria, T.M. Haynes, M.S. Emara, B. Spagnolo, S.R. Datta, M. De Vittorio, B.L. Sabatini, Dynamic illumination of spatially restricted or large brain volumes via a single tapered optical fiber, Nat. Neurosci. 201720 (8) (2017) 1180–1188.
[16] M. Pisanello, F. Pisano, L. Sileo, E. Maglie, E. Bellistri, B. Spagnolo, G. Mandelbaum, B. L. Sabatini, M. De Vittorio, F. Pisanello, Exploiting modal demultiplexing properties of tapered optical fibers for tailored optogenetic stimulation, BioRxiv 2017 (2017).
[17] L. Sileo, M. Pisanello, M.D. Vittorio, F. Pisanello, Fabrication of multipoint light emitting optical fibers for optogenetics, SPIE BiOS 20159305 (2015) 7.
[18] M. Domke, J. Gratt, R. Sroka, Fabrication of homogeneously emitting optical fiber diffusors using fs-laser ablation, SPIE LASE 20169740 (2016) 10.
[19] B. Rubehn, S.B.E. Wolff, P. Tovote, A. Luthi, T. Stieglitz, A polymer-based neural microimplant for optogenetic applications: design and first in vivo study, Lab Chip 201313 (4) (2013) 579–588.
[20] M.J. Gonzalez-Muñoz, I. Meseguer, M.I. Sanchez-Reus, A. Schultz, R. Olivero, J. Benedí, F.J. Sánchez-Muniz, Beer consumption reduces cerebral oxidation caused by aluminum toxicity by normalizing gene expression of tumor necrotic factor alpha and several antioxidant enzymes, Food Chem. Toxicol. 200846 (3) (2008) 1111–1118.
[21] K.-J. Kim, P. Lu, J.T. Culp, P.R. Ohodnicki, Metal–organic framework thin film coated optical fiber sensors: a novel waveguide-based chemical sensing platform, ACS Sensors 2018 (2018).
[22] P.T. Sanecki, K. Gibała, P.M. Skitał, The application of metal deposition in optical sensor technique. The microscale Cu deposition as “electrochemical welding&#x201D, IEEE Sensors J. 201515 (2) (2015) 1275–1279.